EFFECTS OF INGESTED ATMOSPHERIC TURBULENCE ON MEASURED TAIL ROTOR ACOUSTICS

David B. Signor, Gloria K. Yamauchi, and Marianne Mosher
NASA Ames Research Center, Moffett Field, CA 94035-1000

Martin J. Hagen
California Polytechnic State University
San Luis Obispo, CA

Albert R. George
Cornell University, Ithaca, NY

ABSTRACT

Results from an outdoor hover test of a full-scale Lynx tail rotor are presented. The investigation was designed to further the understanding of the acoustics of an isolated tail rotor hovering out-of-ground effect in atmospheric turbulence, without the effects of the main rotor wake or other helicopter components. Measurements include simultaneous rotor performance, noise, inflow, and far-field atmospheric turbulence. Results with grid-generated inflow turbulence are also presented. The effects of turbulence ingestion on rotor noise are quantified. Turbulence ingestion noise is found to be the dominant noise mechanism at locations near the rotor axis. At these locations, the sound radiated by the hovering rotor increases with both increasing atmospheric wind speed and ingested rms turbulent velocity.

NOTATION

a	speed of sound, m/s
b	number of blades (4)
c	blade chord (0.18 m)
C_T/σ	rotor thrust coefficient divided by rotor solidity, rotor thrust/$\rho(\Omega R)^2 bc$
dBA	A-weighted sound pressure level (referenced to 20 μPa)
m	separation distance between rods in the grid (7.6 cm)
M_{tip}	rotor tip Mach number, $\Omega R/a$
N	number of data samples per hot-film time record (2048)
OASPL	over-all sound pressure level, dB (referenced to 20 μPa)
O_r	observer radial distance nondimensionalized by R
R	rotor radius (1.105 m)
u'	rms turbulent velocity, $\sqrt{\frac{1}{N}\sum_{i=1}^{N}(U_i-\bar{u})^2}$, m/s
$\bar{u}$	average velocity, $\frac{1}{N}\sum_{i=1}^{N}U_i$, m/s
U	velocity measured by hot-film probe, m/s
U_∞	atmospheric wind speed measured by cup anemometer, m/s
x	distance downstream from grid, cm
x_o	position of maximum grid-generated turbulence ($5 \le x_o/m \le 15$)
Δt	hot-film signal sample spacing (0.0125 s)

Presented at the AHS 48th Annual Forum, Washington, D.C., June 3-5, 1992.

γ atmospheric wind direction measured from rotor axis ($-30° \leq \gamma \leq 60°$)

Λ eddy length, m

Ω rotor rotational speed, rad/s

ϕ polar angle of observer measured from rotor axis, deg

ρ air density, kg/m^3

θ rotor collective pitch ($3° \leq \theta \leq 15°$)

τ autocorrelation time separation ($j\Delta t$)

Subscripts

f denotes far-field hot-film parameter

n denotes near-field hot-film parameter

INTRODUCTION

Extensive research of rotor noise mechanisms over the past twenty-five years has resulted in a significant increase in the understanding of rotor aeroacoustics. The work by George (Ref. 1) provides a comprehensive review of research on the subject through the late 1970's. JanakiRam (Ref. 2) presents a survey of the "state-of-the-art" in understanding various rotor noise mechanisms and of the development of predictive capabilities throughout the 1970's and 1980's.

Rotor noise is categorized into discrete (or rotational) frequency noise, impulsive noise, and broadband (or random) noise. Individual source mechanisms from the three categories of rotor noise have been investigated both analytically and experimentally with varying degrees of success. JanakiRam and Tadghighi (Ref. 3) evaluated four rotor noise prediction models of varying sophistication used during the late 1980's. The models they considered underpredict experimental data by 10 to 20 dB in general. Inclusion of broadband noise prediction schemes significantly improved correlation with flight test data at higher frequencies.

Broadband noise, in particular, is difficult to predict because the noise is the result of several complex mechanisms. Some broadband noise mechanisms, such as boundary layer trailing-edge noise, are well understood and accurately predicted (George and Chou (Ref. 4)); others are not. A primary contributor to broadband noise which deserves further attention is the turbulence ingestion noise produced by a rotor. A rotor blade interacting with atmospheric turbulence and the turbulent wakes of preceding blades (JanakiRam (Ref. 2)) generates turbulence ingestion noise. The present work focuses on the noise produced by the ingestion of atmospheric turbulence and the contribution of this mechanism to broadband noise.

A lifting rotor accelerates the air and stretches atmospheric eddies passing through the rotor. For a hovering rotor, the blades chop the elongated eddies many times. The velocity fluctuations in the eddies cause fluctuations of the local pressure, lift, and drag on the rotor blades. These unsteady forces are the acoustic source of atmospheric turbulence ingestion noise.

In his review paper, George (Ref. 1) examined many sources of rotor noise generated by a single main rotor helicopter and concluded that ingested atmospheric turbulence is an important source of the overall helicopter noise, in the absence of impulsive noise sources. JanakiRam (Ref. 2) also concluded that turbulence ingestion noise is a significant source of broadband noise when a helicopter is in hover or vertical ascent. JanakiRam notes that as of the late 1970's the most advanced inflow turbulence noise predictive techniques (Homicz and George (Ref. 5), and Amiet (Ref. 6)) had only fair agreement with experimental data. This was attributed to the uncertainty of inflow turbulence statistics and the difficulty of measuring noise from a single source. Also, there was a need for realistic modeling of atmospheric and rotor wake turbulence, as well as the effect of streamline contraction. Simonich et al. (Ref. 7) made significant advances in the understanding of turbulence ingestion noise during the 1980's. Other research in the area of turbulence ingestion noise includes the work by Hanson (Ref. 8), where inlet turbulence measurements were made for a shrouded fan. Pressure transducers mounted on the fan blades provided blade lift spectra. The data revealed a blade lift spectrum of significant level at high frequencies, in addition to narrow band random noise characterized by peaks in the spectrum at multiples of the blade passage frequency.

Paterson and Amiet (Ref. 9) performed the first experimental study of turbulence ingestion effects on a rotor, although not full-scale. The study included testing a model rotor in an anechoic wind tunnel with and without upstream turbulence-generating grids. In addition, outdoor hover testing was conducted. Rotor noise and inflow turbulence were measured for both the

indoor and outdoor portions of the test. Measurement of outdoor inflow turbulence provided an opportunity for Paterson and Amiet (Ref. 9) to use a theory developed by Amiet (Ref. 10) which accounts for anisotropic inflow turbulence in calculating far-field noise. Results from the outdoor hover test of Ref. 9 reveal that the ingestion of atmospheric turbulence was the dominant noise mechanism between 2 and 25 harmonics of the blade passage frequency. The ingested turbulence caused quasi-tonal noise through this frequency range. This effect was attributed to the multiple chopping of long atmospheric eddies. Higher frequency broadband noise was caused by the interaction of smaller eddies with the individual rotor blades. The theory provided reasonable prediction of outdoor hover noise. Low frequency narrowband noise was overpredicted and high frequency broadband noise was underpredicted; the magnitude of the differences depended on observer position. In general, the overall noise level predictions were within 5 dB of measurements. The inclusion of anisotropic inflow effects was essential in obtaining reasonable predictions of turbulence ingestion noise in hover.

Simonich et al. (Ref. 7) conducted a theoretical study to develop a first-principles prediction method for helicopter main rotor noise due to ingestion of atmospheric turbulence. They expanded an existing model which predicts the statistics of the anisotropic turbulence at the rotor plane. Results indicate that decreases in altitude and increases in wind speed increase turbulence ingestion noise. Also, the study concludes turbulence ingestion noise dominates below 30 rotor harmonics and trailing edge noise dominates above 100 harmonics.

Simonich et al. (Ref. 11) conducted an experiment using the same rotor and wind tunnel in Ref. 9 with the specific objective of providing data to validate Amiet's theory (Ref. 7) for anisotropic turbulence. The experiment was conducted in hover. Spectrum characteristics similar to those obtained in the outdoor testing of Ref. 9 were noted. The theory provided reasonable predictions given several measured inflow parameters.

This study advances the work of previous investigations in turbulence ingestion noise by acquiring simultaneous full-scale, hovering tail rotor performance, noise, inflow, and far-field atmospheric measurements.

Knowing the degree of atmospheric stability and the isotropy of the atmospheric turbulence are particularly important when studying rotor turbulence ingestion noise. Unlike the controlled wind tunnel environment, the atmosphere is inherently unsteady and at times unstable. In the atmosphere, turbulence measurement techniques must be appropriate for the existing atmospheric conditions. Analyses such as Ref. 7 require some far-field atmospheric characteristics for calculating turbulence ingestion noise. Experimental validation of such analyses requires simultaneous atmospheric and acoustic measurements.

Direct comparisons of the current work with results from previous investigations were not possible due to significant differences in testing environment. With appropriately applied acoustic scaling laws, however, comparisons with the outdoor hover results of Ref. 9 may be possible. The present work, although not definitive, quantifies the effects of atmospheric turbulence ingestion on hovering rotor noise. The question of whether turbulence ingestion noise is the dominant noise mechanism in hover for a full-scale rotor, as suggested by Simonich et al. (Ref. 11), is examined with current results. In addition, the effects of the rotor on atmospheric eddy lengths and rms turbulent velocities are addressed.

Description of the Experiment

Model

A full-scale Lynx tail rotor was used for this investigation. This rotor consists of four constant-chord, untwisted blades. The rotor hub has conventional flapping and feathering hinges and was 6.1 m above the ground. The tail rotor was mounted on the NASA Ames Tail Rotor Test Rig (TRTR), shown in Fig. 1, at the Outdoor Aerodynamic Research Facility. The rotor drive motor, drive shaft, and right-angle gearbox are mounted inside the horizontal boom, which is mounted on the main vertical support. Additional information about the TRTR and Lynx rotor can be found in Signor et al. (Ref. 12).

Rotor Force Measurements

A strain-gauge balance was used to measure the mean rotor thrust, torque, and vertical force. The balance was mounted between the horizontal support tube and the gearbox mounting bracket.

Flow Measurements

The rotor inflow was measured with a single-element hot-film anemometer and a pitot-static probe. The hot-film and pitot-static probe were mounted on a tower and remained fixed relative to the rotor. The hot-film was horizontal and parallel to the rotor plane.

A 3.6 m- by –3.6 m turbulence grid was installed upstream of the rotor for several runs. The grid was made up of 1.3 cm diameter rods arranged in 7.6 cm square cells. The purpose of the grid was to change the character of the ingested turbulence by introducing small-scale turbulence. Figure 2 shows the locations of the hot-film probe and grid with respect to the rotor. According to Hinze (Ref. 13) and Batchelor (Ref. 14), grid-generated turbulence becomes homogeneous for $x/m \geq 10$, where x is the distance downstream from the grid and m is the cell width. At $x/m = 10$, maximum turbulent velocity is expected. The hot-film and rotor plane were positioned at $x/m = 9.5$ and $x/m = 16.7$, respectively. Therefore, the grid-generated turbulence is expected to be homogeneous at the rotor plane. Figure 3 shows the installation of the grid.

A second single-element hot-film was mounted on a tower located upstream and to the side of the tail rotor. The hot-film was horizontal and parallel to the rotor plane. This probe was used to measure the atmospheric turbulence in the far-field. The probe was 4.7 m above the ground and remained fixed. Figure 4 shows the location of the far-field tower with respect to the rotor.

Constant temperature anemometer bridges powered the hot-film probes. The anemometer signals were linearized. The near-field probe signal was low-pass filtered (filter set at 40 Hz) to remove the blade passage frequency before being digitized. A dynamic signal analyzer with an anti-aliasing filter was used to digitize the data from both probes. No averaging or windowing was used. The data were recorded for 25.6 s at a sample rate of 80 Hz. The probes were calibrated before the experiment, but not before every run. A second calibration performed after the completion of the experiment revealed very little change in the probes' conversion constants or offsets. The data were reduced using the average of the results from the two calibrations.

Atmospheric wind speed and direction were measured using a cup anemometer and a weather vane located on a third tower roughly 46 m upstream of the rotor, 55 m from the rotor axis, and 10 m above the ground. Additionally, the weather station at Naval Air Station Moffett Field recorded several atmospheric parameters hourly. Measurements included air temperature, wind speed, wind direction, barometric pressure, humidity, and cloud conditions. These measurements were recorded 12.8 m above sea level, at a location approximately 1500 m south-east of the Outdoor Aerodynamic Research Facility.

Acoustic Measurements

Nine microphones were typically used to acquire acoustic data. The microphones were placed in an array about the rotor at distances of 2.5, 4.5, and 10 rotor radii away from the hub. All but one of the microphones were at the same height as the rotor. Figure 4 shows the three microphone locations for which measurements are presented in this paper. Acoustic foam was used to substantially reduce reflected rotor noise off the ground, near-field tower, and TRTR (Fig. 1). Wind screens were placed over each microphone to reduce wind-generated noise.

All microphones were calibrated daily using a pistonphone. Two microphone calibrations were recorded each day. The conversion constants from the two recorded calibrations were then averaged; this averaged value served as the conversion constant for each microphone for that particular day. The error associated with this method is on the order of ±1 dB. The data were recorded for 30 s using a 14-track FM tape recorder with a tape speed of 30 ips, giving a frequency span of 20 kHz. Spectra from the acoustic time histories were generated using a dynamic signal analyzer using the rotor 1/rev as an external trigger. The fluctuation in rotor speed was less than 0.2 per cent of full-scale, that is, no more than 2 to 4 rpm. All acoustic data were reduced using a time record of 0.256 s, span of 3.125 kHz, and bandwidth of 5.86 Hz. Each spectrum represents 25 averages (no overlap) of power spectra made with a Hanning window.

The measurements of rotor noise include gear noise from the right-angle gearbox located immediately upstream of the rotor hub. Gear noise, as described by Dale (Ref. 15), appears in the spectra as discrete frequency spikes at some sidebands of the integer harmonics of the gear mesh frequency (37/rev) modulated by the rotor blade passage frequency ($k*37 \pm n*4$ per rev, k and n are integers). The probable cause is modulation of the gear mesh frequency by quasi-periodic disturbances on the rotor blades. Noise was not produced at all

sidebands. Gear noise was removed from the spectra for sidebands of the first three harmonics of the gear mesh frequency. The amplitude of the spectra was interpolated where the spikes were removed. Figure 5 shows a typical correction to an acoustic spectrum.

Configuration and Test Envelope

Data acquisition times were planned for morning hours when the wind speed at the site was low, generally below 5 m/s, in order to simulate hover and obtain high quality acoustic data. The low winds led to generally low turbulence intensities as well, restricting the range of parameters of this experiment.

The test configuration consisted of the TRTR with the microphone array and the near-field and far-field towers. In addition, the turbulence grid was installed for some of the data acquisition runs. The ranges of test parameters are shown in Table 1.

RESULTS AND DISCUSSION

Data Quality

In analyzing the large amount of acoustic and turbulence data, every effort was made to exclude questionable data. Criteria for excluding data, quality of the data, and results from this experiment are discussed below.

The data were limited to those conditions acquired with wind directions of $-30° \le \gamma \le 60°$ (Fig. 4). This avoided blockage effects from the near-field tower and the TRTR on the rotor and hot-film measurements.

In an attempt to compute near- and far-field transverse eddy lengths, a second movable probe was installed at each tower. The movable probe was then traversed upward and away from the fixed probe. Data were typically acquired at seven discrete probe separation distances (0 - 3 m) while holding rotor conditions constant. The transverse eddy length was then computed from the cross-correlation coefficients of the two probes at each tower. This method proved to be inadequate for calculating an accurate transverse eddy length. Data recorded simultaneously from a rake of probes at each tower would have been preferred. Therefore, for this paper, data from only the fixed probe is presented for each tower and no estimate of transverse eddy length is presented.

The longitudinal eddy length at each tower was obtained from respective fixed probe autocorrelations. Autocorrelations were only performed on time histories which appeared stochastic (steady mean value). The autocorrelation is defined as

$$R_j = \frac{1}{N-j} \sum_{i=1}^{N-j} (U_i - \bar{u})(U_{i+j} - \bar{u})$$

The eddy length is defined by

$$\Lambda = \bar{u}\, \Delta t \sum_{j=1}^{q} \frac{R_j}{R_0} \qquad \min(q) \text{ such that } R_q \le 0$$

The far-field eddy lengths were computed using $\bar{u}_f/\cos\gamma$ (far-field wind component adjusted for wind direction). Figure 6 presents a typical normalized autocorrelation. As stated earlier, the probe signals were recorded for 25.6 s. A time record of perhaps thirty minutes for the far-field probes would have been better for determining whether the flow was stationary or not, since the far-field contains turbulent eddies which are complex, large-scale structures. Because the time record lengths were not sufficient to obtain statistically accurate autocorrelations and integral times, the integral scales presented should be considered only as rather coarse estimates. Instrumentation limitations led to the necessity of relatively short time records.

Finally, the sampling rate for the hot-film probes should have been higher, especially for the near-tower probe. Since the probe signals were sampled at 80 Hz and the near-tower signal was low-pass filtered at 40 Hz before being recorded, the frequency content beyond 40 Hz is not available. This prevents a determination of the turbulence spectrum above 40 Hz and prevents a determination of the filter effect on the turbulence level or length scale. In a similar experiment, however, Paterson and Amiet (Ref. 9) found the error in overall rms turbulence level due to low-pass filtering to be less than 10 per cent.

Atmospheric Measurements

Quantifying the magnitude of turbulence ingestion noise for this test requires knowledge of the atmospheric turbulent structure, which is very complicated. The structure depends upon the wind profile and upstream conditions, terrain roughness and shear,

fluxes of moisture and thermal energy, cloud cover, time of day, and other factors. Depending on these factors the turbulent velocities can be moderately or severely anisotropic (especially in stably stratified conditions) . In addition, inhomogeneous large eddy structures often include significant intermittency (Thomson and Henderson (Ref. 16), Wilson (Ref. 17)). The environmental turbulence is then distorted while being convected into a rotor (Simonich et al. (Ref. 7)). Since complete characterization of the turbulence was beyond the scope of this experiment, only a few basic characteristics were measured at the near-field and far-field locations.

The upstream wind conditions at the Outdoor Aerodynamic Research Facility generally begin over San Francisco Bay. From the shoreline, the upstream wind flows over one kilometer of terrain consisting of long grass with some shrubs, isolated trees, and berms. Although the atmosphere appeared to be stably stratified at higher altitudes, the atmosphere at the rotor height was likely neutral or slightly unstable during the testing periods due to mechanical mixing from terrain roughness. The general character of the turbulence at any location in the atmospheric boundary layer is determined by the stability of the atmosphere relative to the turbulence generated by shear stress. If the atmosphere is neutral to slightly buoyant, the turbulence will be similar to that in an aerodynamic boundary layer. This was checked for conditions during this test by estimating the dimensionless Richardson number. Following Panofsky and Dutton (Ref. 18), the Turner classes of the flow were estimated from the Moffett Field weather and solar data to find the approximate Monin-Obukhov lengths and the Richardson numbers. The range of estimated Monin-Obukhov lengths was approximately –10 to –25 m and the range of Richardson numbers was approximately –0.06 to –0.25. Thus, the results of this method indicate near neutral to slightly unstable conditions. This was consistent with the hot-film measurements and indicates that the assumption of isotropic turbulence is a reasonable first approximation far from the rotor. Figure 7 shows a typical near-field hot-film spectrum compared with the von Karman spectrum. The spectra are power spectral densities presented in a format, F_{11}, used by Coffen (Ref. 19). The data appear to exhibit the same basic character as the von Karman spectrum.

Far-Field. Far-field length scales shown in Fig. 8 are of the order of the measurement height. Thus, these data are consistent with length scales that are of the expected order of magnitude for a neutral to slightly buoyant boundary layer. The eddy lengths at the lowest wind speeds are low because there is very little mechanical mixing. In Fig. 8, the eddy lengths initially increase with increasing wind speed. The wind speed component measured by the far-field probe has been adjusted for wind direction in order to arrive at the total magnitude. At moderate wind speeds the eddy lengths become more independent of wind speed. At wind speeds higher than shown in Fig. 8, the average eddy length would be expected to be about 4.7 m. Nominally, the largest eddy length possible is of the order of the atmospheric boundary layer thickness, which is approximately 1-2 km according to Panofsky and Dutton (Ref. 18).

The measured atmospheric rms turbulent velocities, u'_f, corresponding to the eddy lengths in Fig. 8 are shown in Fig. 9. The primary cause for u'_f increasing with wind speed is development of the boundary layer with increasing wind speed.

Near-Field. The stretching of the eddies as they are accelerated through the rotor is shown in Fig. 10. The grid was not installed for these conditions. The amount of eddy stretching is one measure of how the rotor alters the surrounding atmospheric turbulence prior to ingesting the turbulence. The length and speed of the ingested eddies determine the number of times the eddy will be chopped by the rotor blades. The average ratio of near- to far-field longitudinal eddy lengths is 2.6. A significant number of stretching ratios are less than one, however. This is because measurements were made in an Eulerian sense, not Lagrangian—individual eddies were not tracked as they traveled from the far-field and became distorted by the rotor. Therefore, the eddies entering the rotor should in general be longer than the far-field eddies, but there will be exceptions. The magnitude of the ingested eddy lengths is shown in Fig. 11. No discernible effects of M_{tip} or rotor collective pitch on eddy length were observed.

Acoustic Measurements

Acoustics results are shown for three of the nine observer positions (Table 2 and Fig. 4). The primary measurement, Microphone 9, was 4.5 rotor radii from the rotor on the rotor axis. Measurements at this location show the greatest effect of atmospheric turbulence ingestion. Microphones 2 and 6 were placed 45° and 90° (in-plane) from the rotor axis, respectively. Background noise measurements were typically at least 20 dB below the acoustic measurements of the rotor.

General Characteristics. Figure 5 shows the averaged spectrum from Microphone 9 with and without the gear noise removed. Several aspects of this spectrum are characteristic of the broadband noise measured in this experiment. The spectrum contains 28 distinct rotor blade passage harmonics rising above the broadband noise. For a hovering rotor, two mechanisms which produce peaks at the blade passage frequency are steady loading noise and turbulence ingestion noise. Peaks from steady loading noise diminish with increasing frequency much faster than in this example. The peaks in the measured spectrum are very narrow at the lower frequencies and increase in width as the frequency increases; this is a characteristic of turbulence ingestion noise (Homicz and George (Ref. 5)). Another possible cause of widening peaks is unsteadiness in the rotor speed; however, as explained earlier, the rotor speed was found to be very steady. Also, the peaks identified with the gear noise do not widen at the higher frequencies. Therefore, the widening of the peaks in the spectrum is most likely caused by turbulence ingestion. Additional spectra from Microphone 9 acquired for various rotor and atmospheric conditions exhibit similar characteristics. In contrast, spectra from Microphone 6 (in-plane location) exhibit slightly different characteristics, as shown in Fig. 12. The amplitudes of the first two or three blade passage harmonics are larger and can be attributed to thickness noise. Amplitudes diminish quickly for the first three or four harmonics; levels of all harmonics above about the fourth are lower at this location. The existence of distinct and broadening peaks in the spectra out to 3 kHz indicate some noise is radiating from the turbulence ingestion; however, this noise is about 40 dB below the fundamental and thus contributes little to the sound level in the plane of the rotor either in OASPL or dBA measurements. Spectra from Microphone 2 (45° from the rotor axis) are similar to Microphone 9 spectra.

Atmospheric Turbulence Effects. Variations in atmospheric turbulence are expected to cause changes in the sound measurements when turbulence ingestion is a major sound producing mechanism. The structure of the inflow turbulence incident on the rotor will influence the nature of the blade lift fluctuations and thus the radiated sound. If the time records of the probes were long enough to obtain a statistical average and short enough for the turbulence characteristics to be quasi-stationary, the near- and far-field measured turbulence characteristics should be clearly related. As shown in Figs. 8-11, however, much scatter exists in the turbulence measurements. In this section, therefore, acoustic measurements will only be related to estimates of turbulence characteristics made in the near-field.

When a rotor interacts with atmospheric turbulence, the turbulence produces fluctuating pressures on the rotor blades leading to fluctuating lift and drag. These pressure fluctuations radiate away from the rotor as sound. Most likely, the fluctuating lift will exceed the fluctuating drag. If this happens, more sound will radiate perpendicular to the blade in the direction of the rotor axis than parallel to the blade close to the plane of the rotor. Also, higher rms turbulent velocities are expected to produce higher pressure fluctuations and higher radiated sound levels than lower rms turbulent velocities. Figures 13a - 13d show the effects of rms turbulent velocity in the near-field, u'_n, on the sound radiated by the rotor. The grid was not present. The metric dBA was chosen over OASPL because dBA gives more weight to the frequencies between 1 and 4 kHz. Thus, more weight is given to the frequencies where turbulence ingestion noise is more significant than thickness or steady loading noise and to the frequencies where humans are most sensitive. Figure 13a shows measurements for Microphone 9. Levels increase with increasing rotor collective pitch. Scatter in the data appears to be about 3 dB. For a fixed collective ($\theta = 7°$), the dBA levels tend to increase slightly with increasing turbulence levels. Trends for Microphone 2 (Fig. 13b), at 45° from the rotor axis, are similar to the Microphone 9 trends with scatter up to 5 dB. In the plane of the rotor, measurements made with Microphone 6 indicate no trend with u'_n (Fig. 13c). At this location, thickness noise dominates the radiated noise and is manifested mainly in the first few rotor harmonics. Figure 13d shows measured noise as a function of inflow turbulence for Microphone 9 at $M_{tip} = 0.62$ and no grid present. Compared to the $M_{tip} = 0.52$ case (Fig. 13a), no trends with u'_n are observed. Instead measurements for each collective pitch lie in a band about 3 dB wide. This same banding of dBA occurs at the other two microphone locations. Figure 14 shows spectra from two points in Fig. 13a with a collective pitch of 7° and two different values for u'_n. All other conditions for the two points are similar, except the atmospheric wind speed. The wind speeds are 0.66 and 3.85 m/s corresponding to the smaller and larger values of u'_n, respectively. With higher u'_n, the amplitude of the lower frequency rotor blade passage harmonics is greater than for the lower u'_n case; the amplitudes of the higher frequency harmonics are about the same. Also, with higher rms turbulent velocities, the broadband noise floor increases, about 2 dB at the lower frequencies and about 5 dB at the higher frequencies shown.

Eddy length may also affect the turbulence ingestion noise produced by a rotor. The rotor will chop a

long eddy for a longer period than a short eddy, which could produce more tonal noise. Figure 15 shows measurements from Microphone 9 for $M_{tip} = 0.52$ with no grid present. Levels increase with increasing rotor collective pitch. Scatter in the data appears to be about 5 dB and is greater than the scatter when dBA is plotted against u'_n. For a fixed collective, no distinct effect of eddy length is observed. Measurements made with Microphone 2 show similar trends with greater scatter. Microphone 6 measurements also show no dependence on eddy length. All acoustic measurements made with $M_{tip} = 0.62$ show no dependence on eddy length. Figure 16 shows spectra from two points in Fig. 15 with a rotor collective pitch of 7° and two different values of the eddy length, Λ_n. All other conditions are similar. No significant difference between the two spectra is observed. Because of the high rpm of this tail rotor (blade passage frequencies of 102-124 Hz) and the ingested eddy size (2 to 20 m), the rotor is expected to chop the eddy 80 to 800 times. Chopping an eddy 80 times is sufficient to produce fairly coherent sound; increasing the number of chops above 80 may have insignificant effect on the coherence. Thus noise produced by the tail rotor chopping of the longest eddies may be only slightly more coherent than the noise produced by the rotor chopping the shortest eddies in this experiment.

The atmospheric wind speed is the other basic characteristic of the atmospheric turbulence that was measured. Both rms turbulent velocities and eddy length exhibit some correlation with wind speed. Radiated sound also correlates with wind speed. Figure 17 shows Microphone 9 measurements for $M_{tip} = 0.52$ with no grid present. Levels increase with increasing rotor collective pitch. Scatter in the data appears to be about 3 dB. For a fixed collective ($\theta = 7°$), the dBA levels tend to increase with increasing wind speeds. As with rms turbulent velocities and eddy lengths, trends for Microphone 2 are similar to those on the rotor axis and contain more scatter. No dependence of dBA on wind speed, U_∞, was observed for Microphone 6. Measurements for all three locations made at $M_{tip} = 0.62$ show no dependence on U_∞.

Rotor Collective Pitch. According to current theories, pressure disturbances on the rotor blade and radiated sound due to turbulence ingestion are independent of the steady lift of the rotor blade. However, in all the measurements examined above, the sound level in dBA increased with increasing rotor collective. Figure 18 shows spectra from two points in Fig. 13d for $M_{tip} = 0.62$. Spectra are shown for collectives of 3 and 15° corresponding to C_T/σ of 0.004 and 0.076, respectively. The amplitudes of the rotor blade passage harmonics and dBA (Fig.13d) are about 12 dB higher with the higher collective pitch. The broadband floor is about 2 dB higher at the lower frequencies and the difference increases to about 15 dB at the higher frequencies.

Turbulence Grid. A grid in a fluid stream creates eddies with length scale on the order of the grid cell spacing. These eddies decay far downstream of the grid. The rotor was in the near downstream region of the grid where the small, grid-generated eddies had decayed but were still present and the larger atmospheric eddies had not decayed much. Inserting the grid changed the turbulence ingested by the rotor. The exact nature of this change was not documented. The grid changed the turbulence by adding small-scale turbulence to the existing atmospheric turbulence. This change in turbulence is expected to increase the broadband floor at the higher end of the noise spectra examined in this investigation. Figure 19 shows Microphone 9 measurements for $M_{tip} = 0.62$ with and without the grid present for $\theta = 3$, 7, and 15°. Acoustic measurements made with the grid present are consistently higher, with the difference increasing for higher collective. Measured values of u'_n are not available for conditions with the grid. Batchelor (Ref. 14) provides an equation for estimating the rms turbulent velocity downstream of a grid.

$$\left(\frac{\bar{u}}{u'}\right)^2 = 134\left(\frac{x}{m} - \frac{x_o}{m}\right)$$

The calculated rms turbulent velocities range from 0.067 to 0.26, 0.12 to 0.36, and 0.19 to 0.53 for $\theta = 3$, 7, and 15°, respectively. The error in estimating x_o/m has been included in these calculations, i.e., $5 \le x_o/m \le 15$. Figure 20 shows two spectra, with and without grid, representing two points in Fig. 19 for a collective pitch of 3°. Amplitudes of the rotor blade passage harmonics are 3 to 5 dB higher for most harmonics when the grid is present. The amplitude of the broadband floor is also higher with the grid, about 3 dB at low frequencies and about 5 dB at higher frequencies.

CONCLUSIONS

In order to determine the effects of atmospheric turbulence ingestion on rotor acoustics, numerous characteristics of the atmosphere must be measured simultaneously, in addition to the rotor radiated noise. To date, no single experiment has included acquisition of all the necessary and difficult measurements.

Atmospheric stability and isotropy of the turbulence appear to be the primary atmospheric characteristics which must be established. Atmospheric conditions during this experiment were near neutral or slightly unstable. Determining appropriate hot-film time record lengths is also problematical. The records must be long enough to be stochastic, but short enough for the turbulence characteristics to be quasi-stationary. This involves observing, acquiring, and analyzing extensive amounts of atmospheric data at the test site before and during acquisition of rotor acoustic measurements. This study, although by no means comprehensive, offers the following conclusions.

Acoustic Measurements

1. The data suggest that atmospheric turbulence ingestion noise is the dominant noise mechanism near the rotor axis for a hovering rotor.

2. Increasing rotor thrust increases sound radiated from atmospheric turbulence ingestion by the rotor.

3. In directions along the rotor axis or at 45° to the axis, sound radiated by the rotor in hover increases both with increasing atmospheric wind speed and ingested rms turbulent velocity.

4. In the plane of the rotor, sound radiated by a rotor in hover is insensitive to changes in atmospheric wind speed or ingested rms turbulent velocity.

5. In directions along the rotor axis, 45° to the axis, and 90° to the axis, the sound radiated is insensitive to changes in ingested eddy lengths when the eddy is long enough to be chopped at least 80 times.

6. At locations on the rotor axis, widening of spikes in the noise spectrum at higher frequencies (1500 - 3000 Hz) is caused by atmospheric turbulence ingestion noise.

7. Measured noise levels with the turbulence-generating grid are consistently higher than without the turbulence-generating grid.

Atmospheric Measurements

8. Near-field atmospheric turbulence data exhibit characteristics of a von Karman spectrum.

9. Far-field axial length scales are of the order of the measurement height, as expected.

10. Far-field rms turbulent velocities increase with atmospheric wind speed (over the range of these test conditions).

11. The average ratio of near- to far-field eddy lengths is 2.6.

ACKNOWLEDGMENTS

The authors would like to thank Dr. Charles Smith of NASA Ames for his helpful comments and suggestions. We also appreciate the informative discussions with Dr. Dennis Thomson of Pennsylvania State University, Dr. Doug Westphal of NASA Ames Research Center, and Mr. Mike Marcolini of NASA Langley Research Center.

REFERENCES

[1]George, A. R., "Helicopter Noise: State-of-the-Art," *J. Aircraft*, Vol. 15, (11), pp. 707-715, November 1978.

[2]JanakiRam, R. D., "Aeroacoustics of Rotorcraft," AGARD FDP Special Course: Aerodynamics of Rotorcraft, NASA Ames Research Center, May 1990.

[3]George, A. R. and Chou, S. T.," Broadband Rotor Noise Analysis," NASA CR-3797, April 1984.

[4]JanakiRam, R. D. and Tadghighi, H., "Rotor Noise Prediction and Validation," American Helicopter Society 43rd Annual Forum, St. Louis, Missouri, May 1987.

[5]Homicz, G. F. and George, A. R., "Broadband and Discrete Frequency Radiation for Subsonic Rotors," *J. Sound and Vibration*, Vol. 36, (2), pp. 151-177, 1974.

[6]Amiet, R. K., "Noise Produced by Turbulent Inflow into a Propeller or Helicopter Rotor," *AIAA J.*, Vol. 15, (3), March 1977.

[7]Simonich, J. C., Amiet, R. K., Schlinker, R. H. and Greitzer, E. M., "Helicopter Rotor Noise Due to Ingestion of Atmospheric Turbulence," NASA CR-3973, May 1986.

[8]Hanson, D. B., "Spectrum of Rotor Noise Caused by Atmospheric Turbulence," *J. Acoustical Society of America*, Vol. 56, (1), July 1974.

[9]Paterson, R. W. and Amiet, R. K., "Noise of a Model Helicopter Rotor Due to Ingestion of Turbulence," NASA CR-3213, November 1979.

[10]Amiet, R. K., "Noise Produced by Turbulent Inflow into a Propeller or Helicopter Rotor," *AIAA J.*, Vol. 15, (3), March 1977.

[11]Simonich, J. C., Schlinker, R. H. and Amiet, R. K., "Experimental Assessment of Helicopter Rotor Turbulence Ingestion Noise in Hover," NASA CR-181792, June 1989.

[12]Signor, D., Yamauchi, G., Smith, C. and Hagen, M., "Performance and Loads Data from an Outdoor Hover Test of a Lynx Tail Rotor," NASA TM-101057, June 1989.

[13]Hinze, J. O., *Turbulence*, McGraw Hill, Inc., 1975, pp. 259-277.

[14]Batchelor, G. K., *The Theory of Homogeneous Turbulence*, Cambridge University Press, 1967, pp. 133-168.

[15]Dale, A. K., "Gear Noise and The Sideband Phenomenon," ASME Design Engineering Technical Conference, Cambridge, Massachusetts, October 7-10, 1984.

[16]Thomson, D. W. and Henderson, H. W., "Definition of Local Atmospheric Attractors using Measurements Made with Surface-based Remote Sensing Systems," First Experimental Chaos Conference, Arlington, Virginia, October 1-3, 1991.

[17]Wilson, D. K., "Propagation of Sound Through the Fluctuating Atmosphere," Second International Congress on Recent Developments in Air- & Structure-Borne Sound and Vibration, Auburn, Alabama, March 4-6, 1992.

[18]Panofsky, H. A. and Dutton, J. A., *Atmospheric Turbulence*, John Wiley & Sons, 1984, pp. 87, 139-140.

[19]Coffen, C., "Tilt Rotor Hover Aeroacoustics," M.S. Thesis, Cornell University, May 1992.

Table 1 Range of test parameters

Rotor collective, θ	3° to 15°
C_T/σ	0.004 to 0.076
Tip Mach number, M_{tip}	0.52, 0.62
Atmospheric wind direction, γ	–30° to 60°
Atmospheric wind speed U_∞	0.4 to 6 m/s
Far-field eddy length, Λ_f	0.8 to 12 m
Average inflow velocity, $\bar{u}_n$	2.5 to 8.0 m/s
Grid	with, without

Table 2 Microphone locations

Microphone	O_r	ϕ
2	2.5	45°
6	4.5	90°
9	4.5	0°

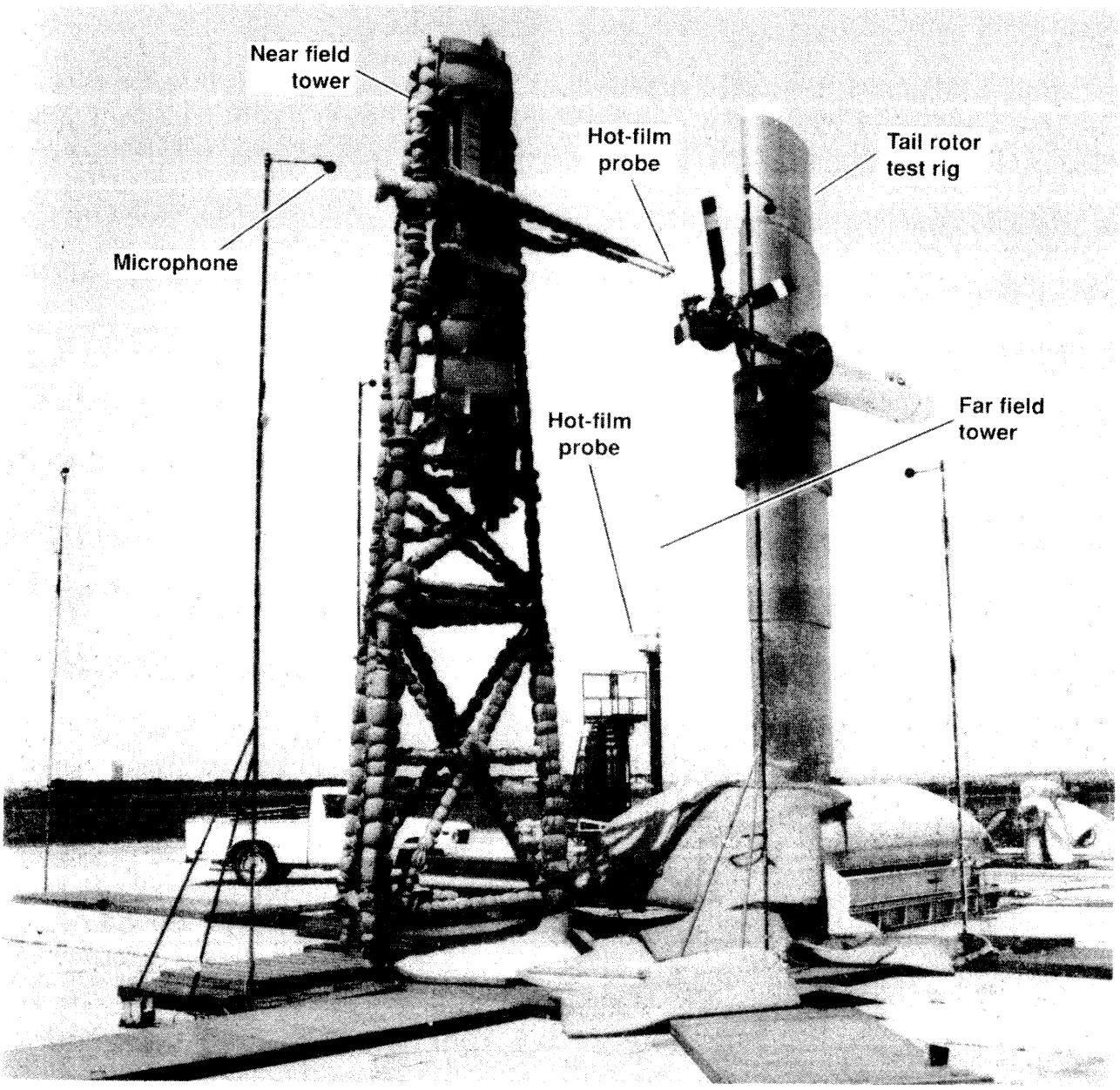

Fig. 1 Experimental set-up.

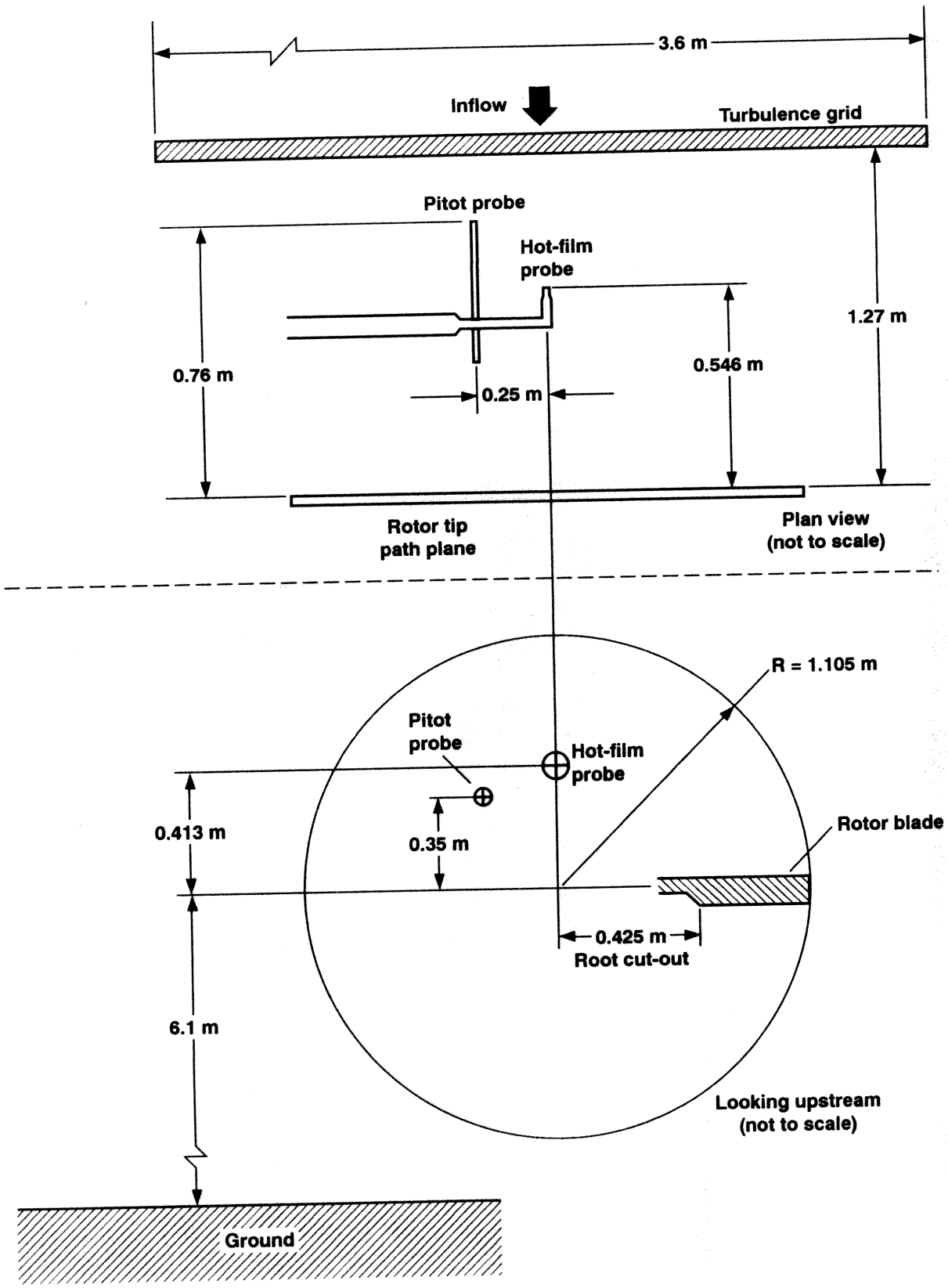

Fig 2 Near-field hot-film probe and grid location.

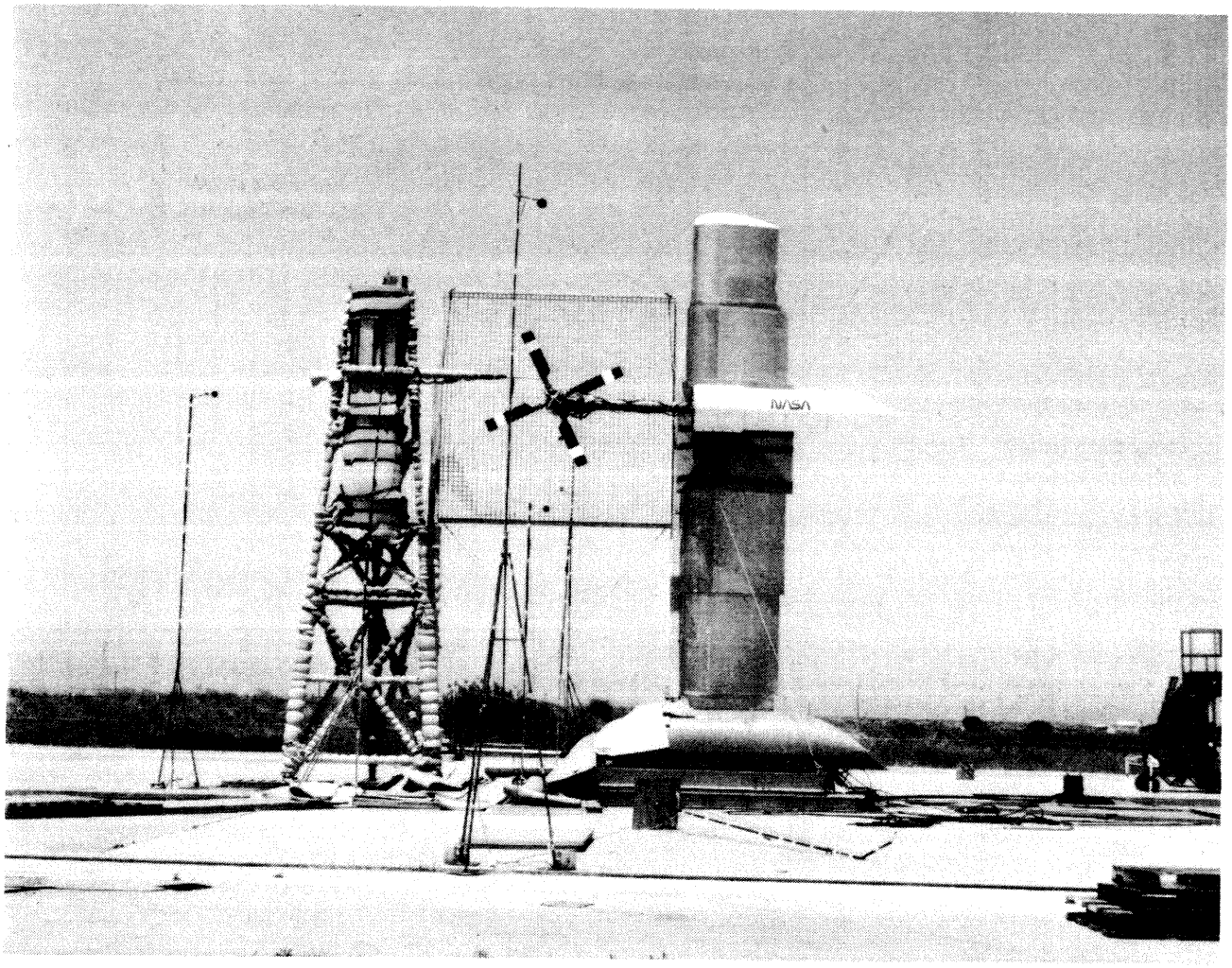

Fig. 3 Turbulence-generating grid installation.

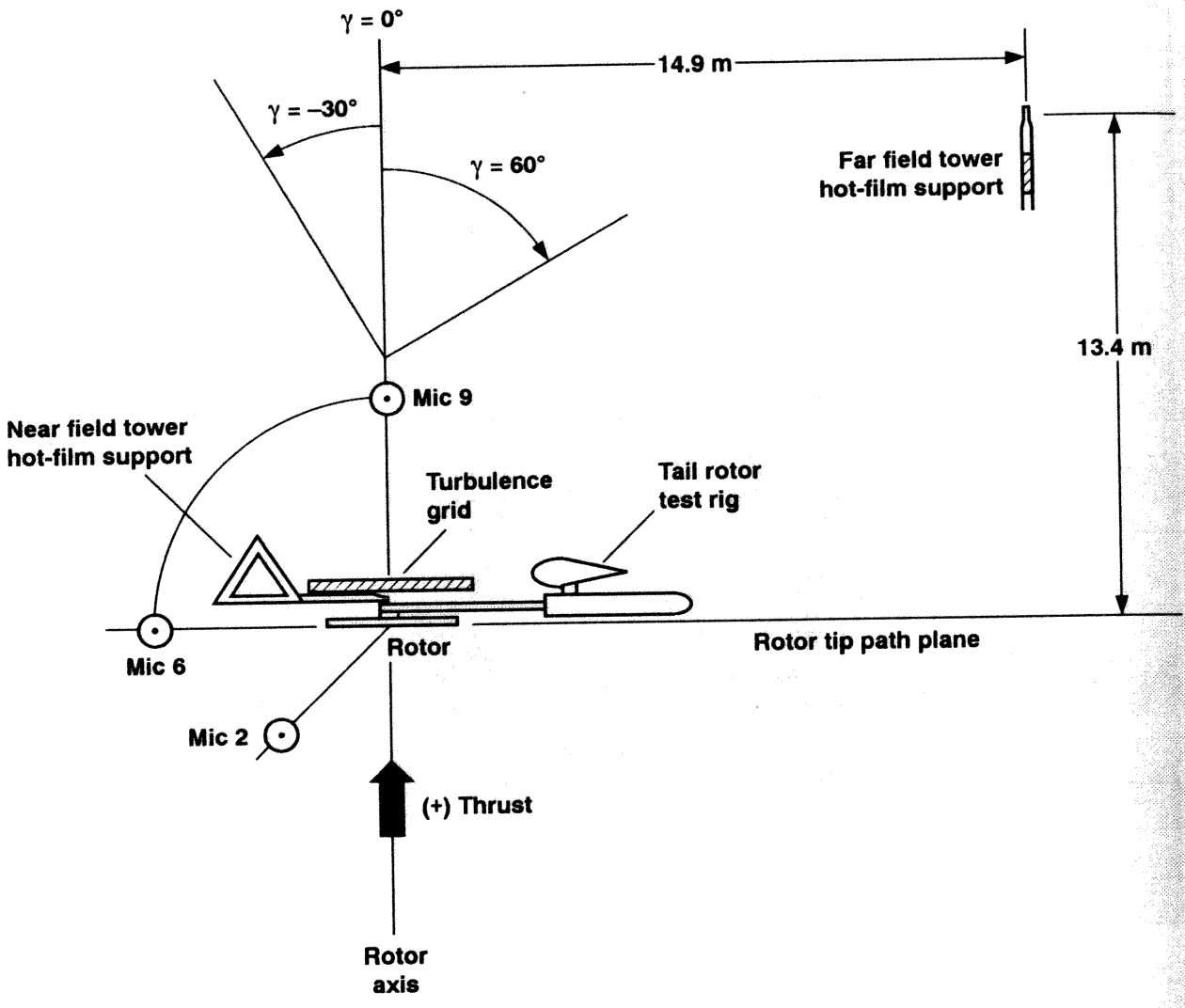

Fig. 4 Plan view of experimental set-up.

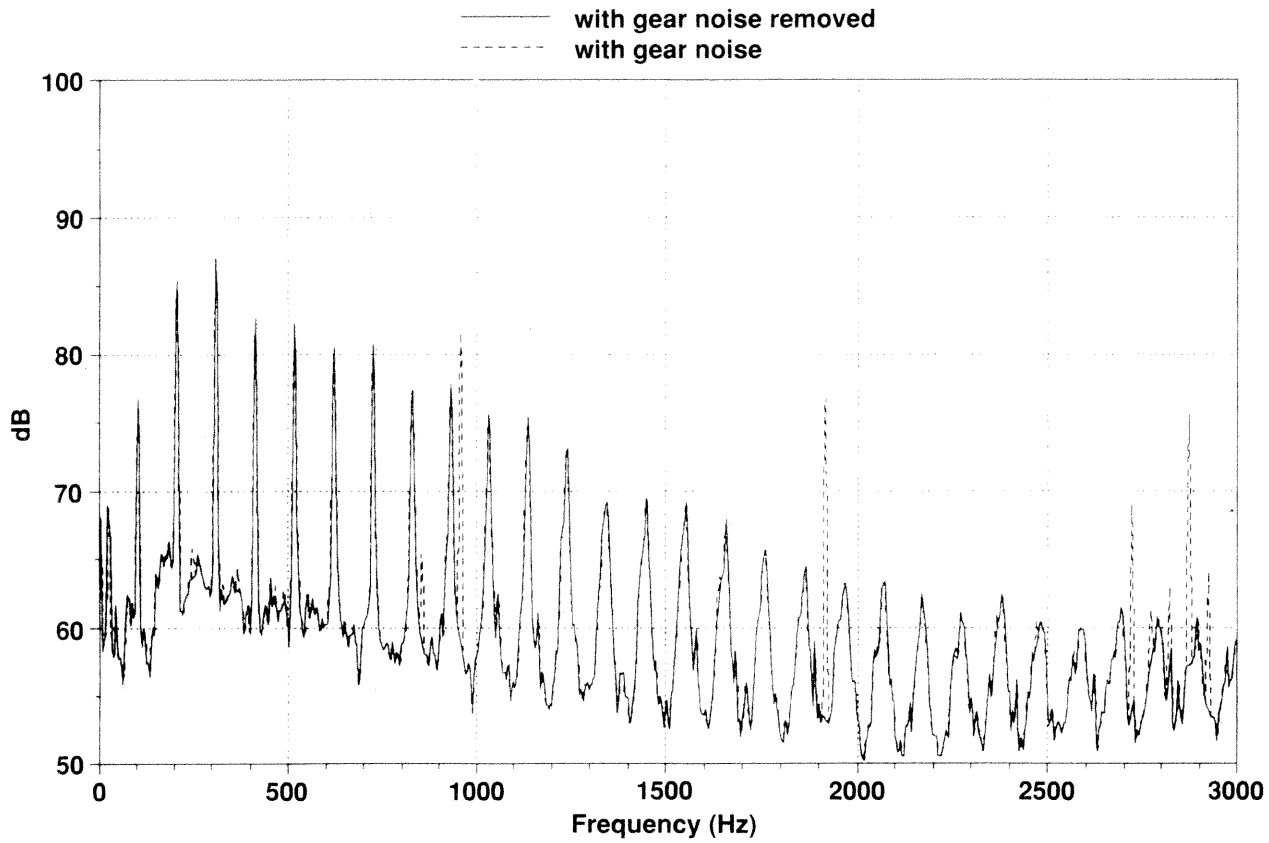

Fig. 5 Power spectrum showing effect of gear noise removal at microphone 9, $O_r = 4.5$, $\phi = 0°$, without grid, $M_{tip} = 0.52$, $\theta = 7°$, $U_\infty = 0.48$ m/s, $u'_n = 0.083$ m/s, $\Lambda_n = 7.2$ m, $\bar{u}_n = 3.96$ m/s.

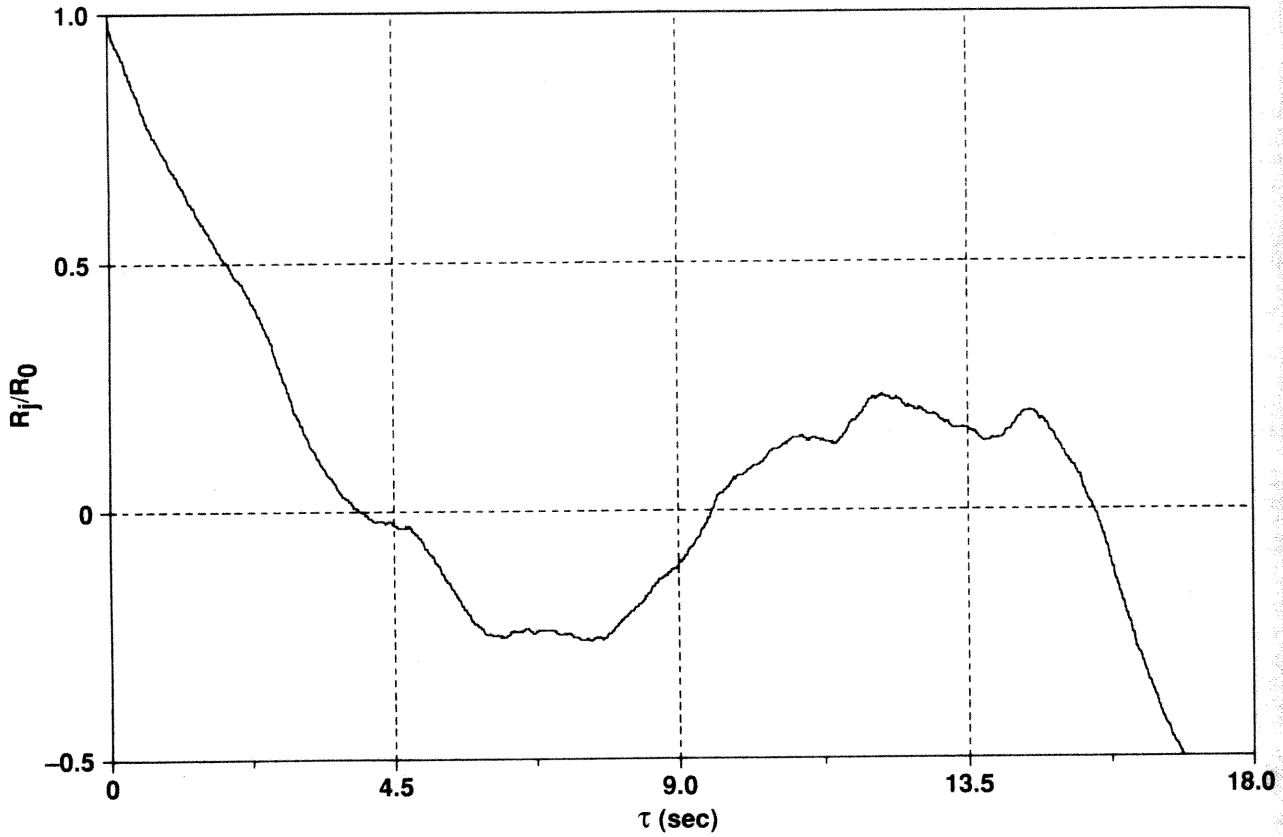

Fig. 6 Example of autocorrelation without grid, $M_{tip} = 0.52$, $\theta = 7°$, $U_\infty = 0.48$ m/s, $u'_n = 0.083$ m/s, $\Lambda_n = 7.2$ m, $\bar{u}_n = 3.96$ m/s.

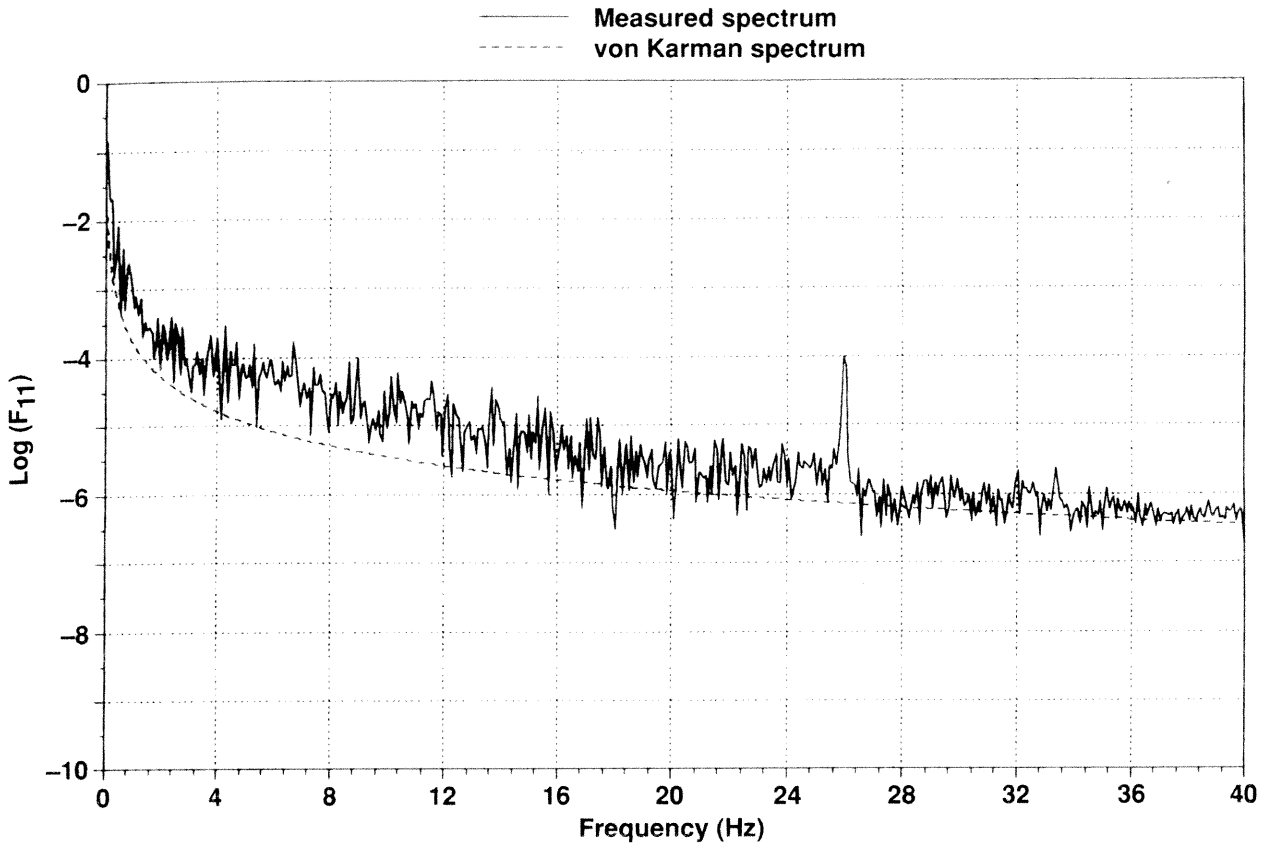

Fig. 7 Comparison of von Karman spectrum with measured turbulence spectrum, $M_{tip} = 0.52$, $\theta = 7°$, $U_\infty = 0.48$ m/s, $u'_n = 0.083$ m/s, $\Lambda_n = 7.2$ m, $\bar{u}_n = 3.96$ m/s.

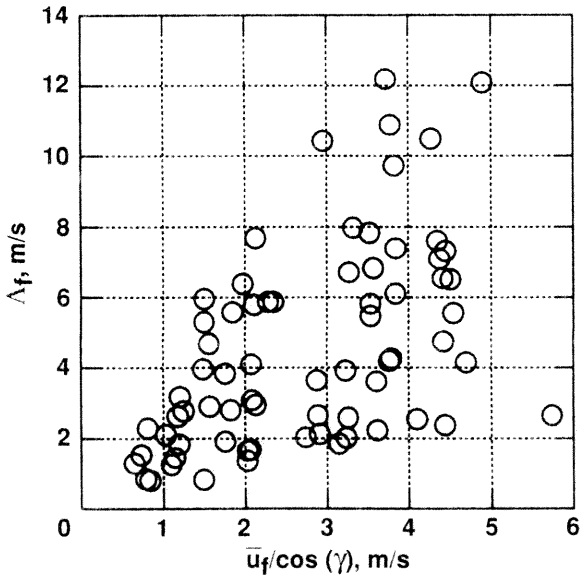

Fig. 8 Far-field eddy lengths.

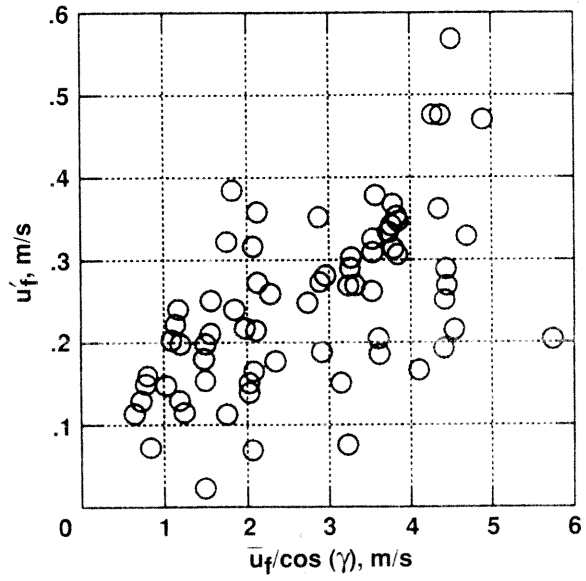

Fig. 9 Far-field rms turbulent velocity.

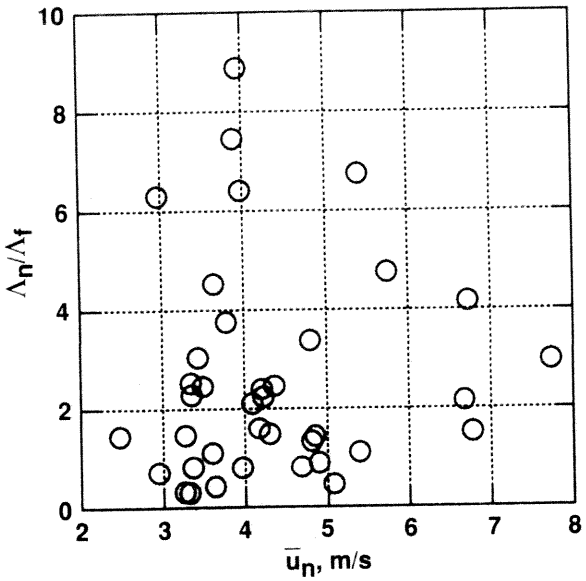

Fig. 10 Longitudinal eddy length stretching ratio.

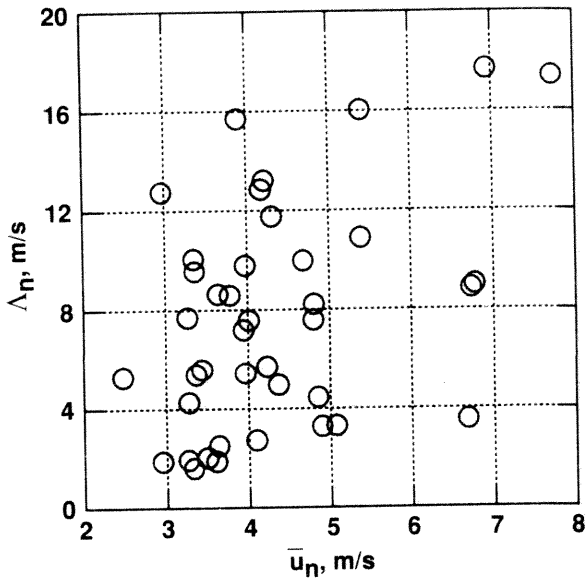

Fig. 11 Near-field longitudinal eddy length.

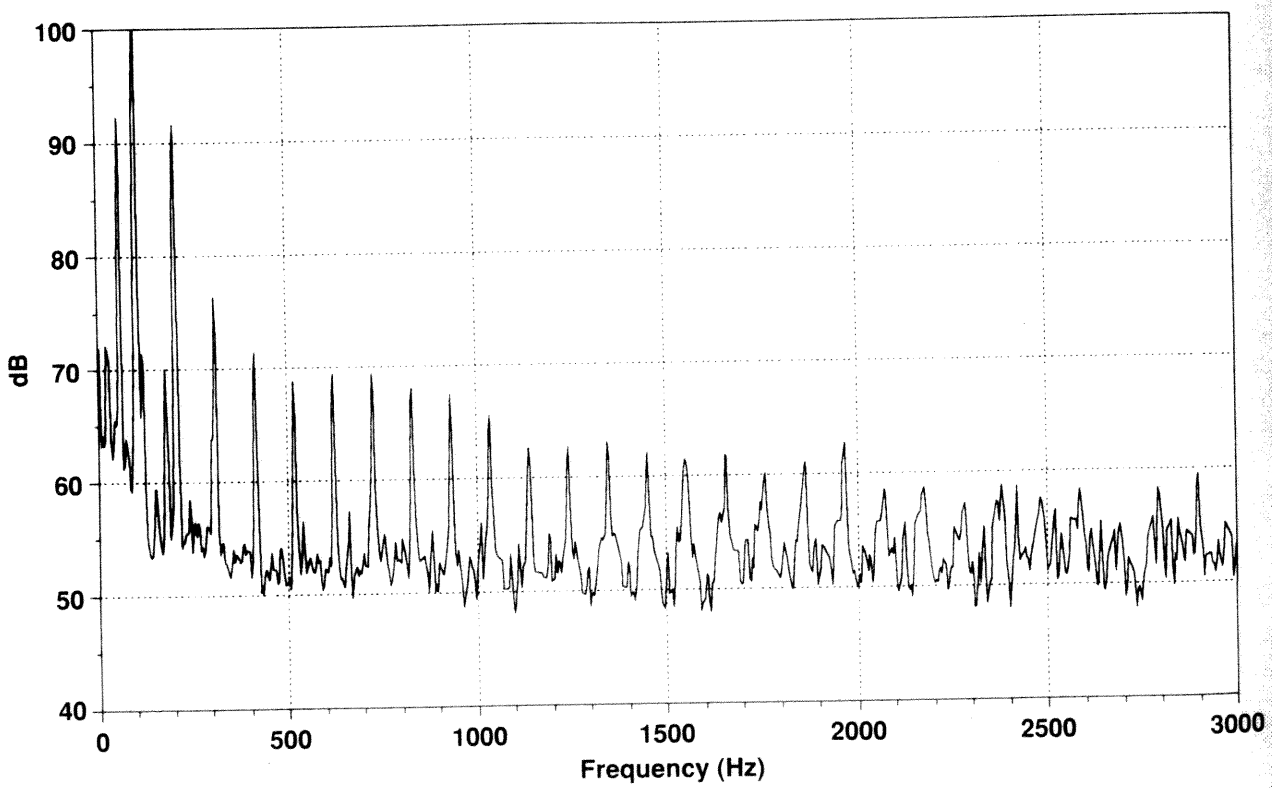

Fig. 12 Power spectrum at microphone 6, $O_r = 4.5$, $\phi = 90°$, without grid, $M_{tip} = 0.52$, $\theta = 7°$, $U_\infty = 0.48$ m/s, $u'_n = 0.083$ m/s, $\Lambda_n = 7.2$ m, $\bar{u}_n = 3.96$ m/s.

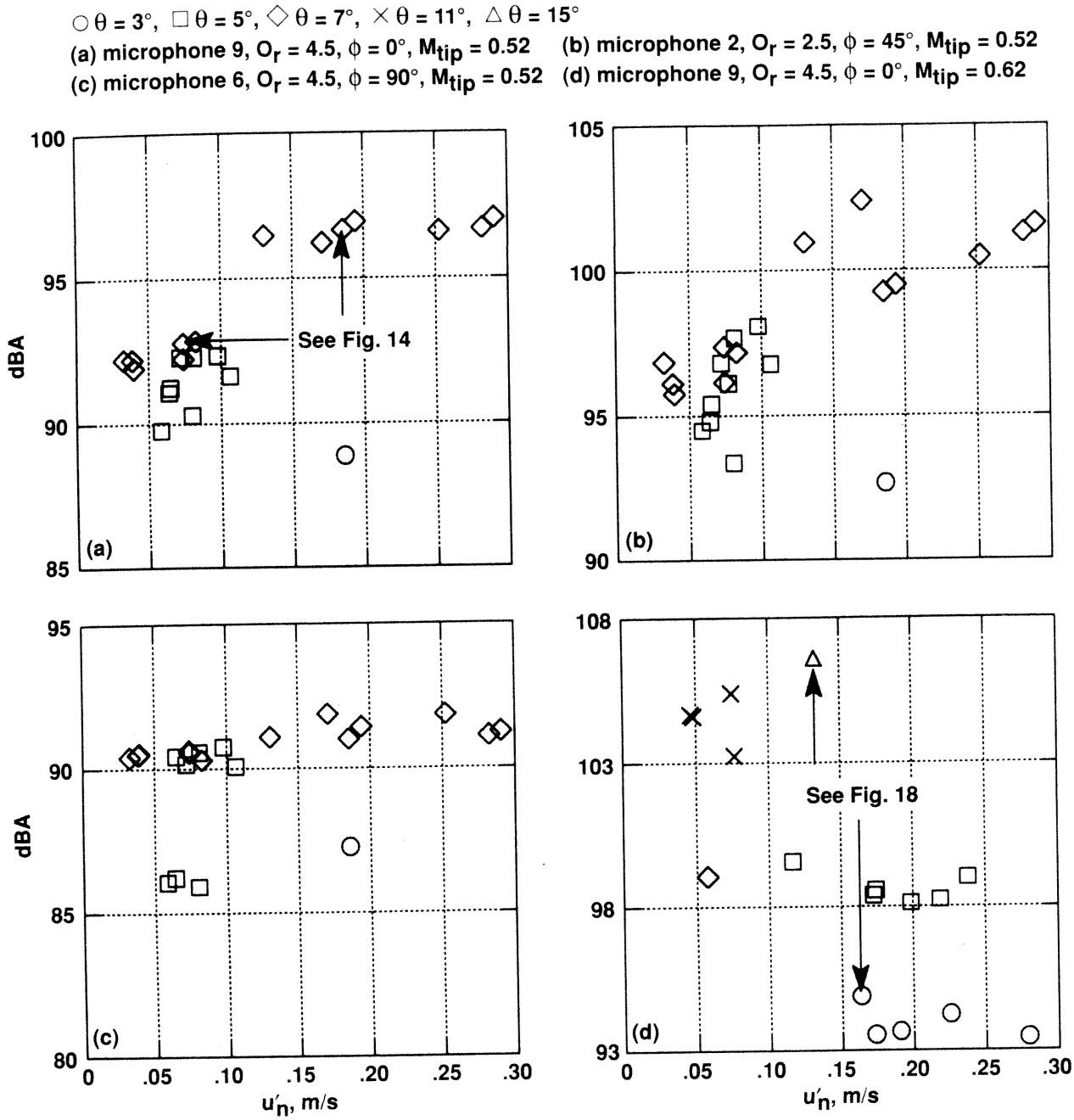

Fig. 13 Measured sound level variation with rms turbulent velocity.

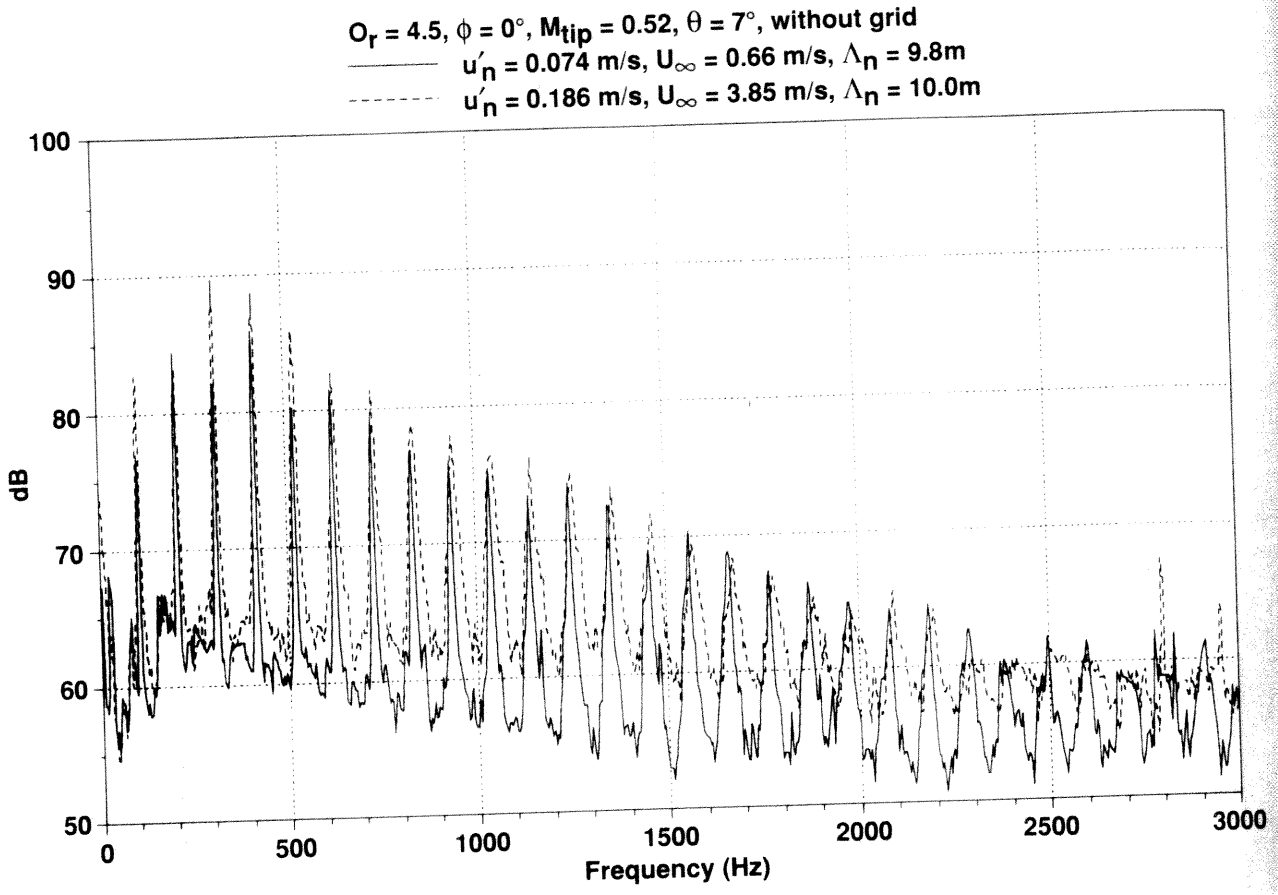

Fig. 14 Effect of near-field rms turbulent velocity on acoustic power spectra at microphone 9.

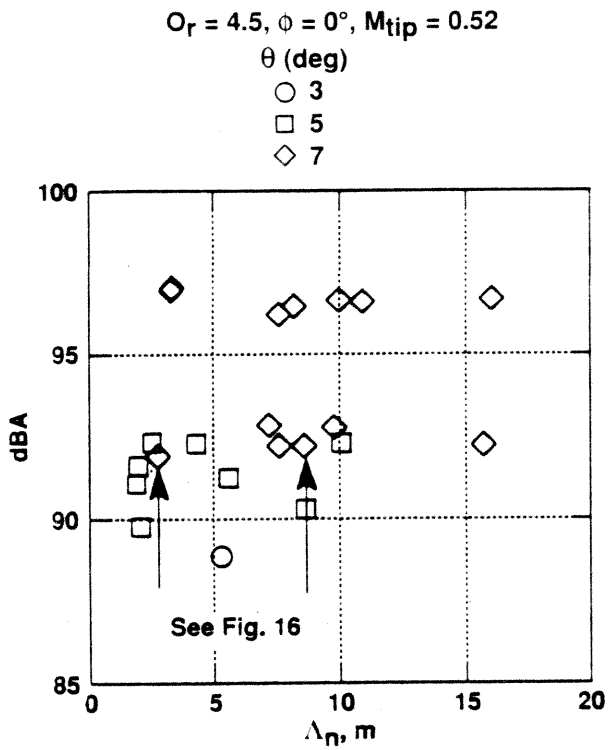

Fig. 15 Measured sound level variation with near-field eddy length without grid at microphone 9.

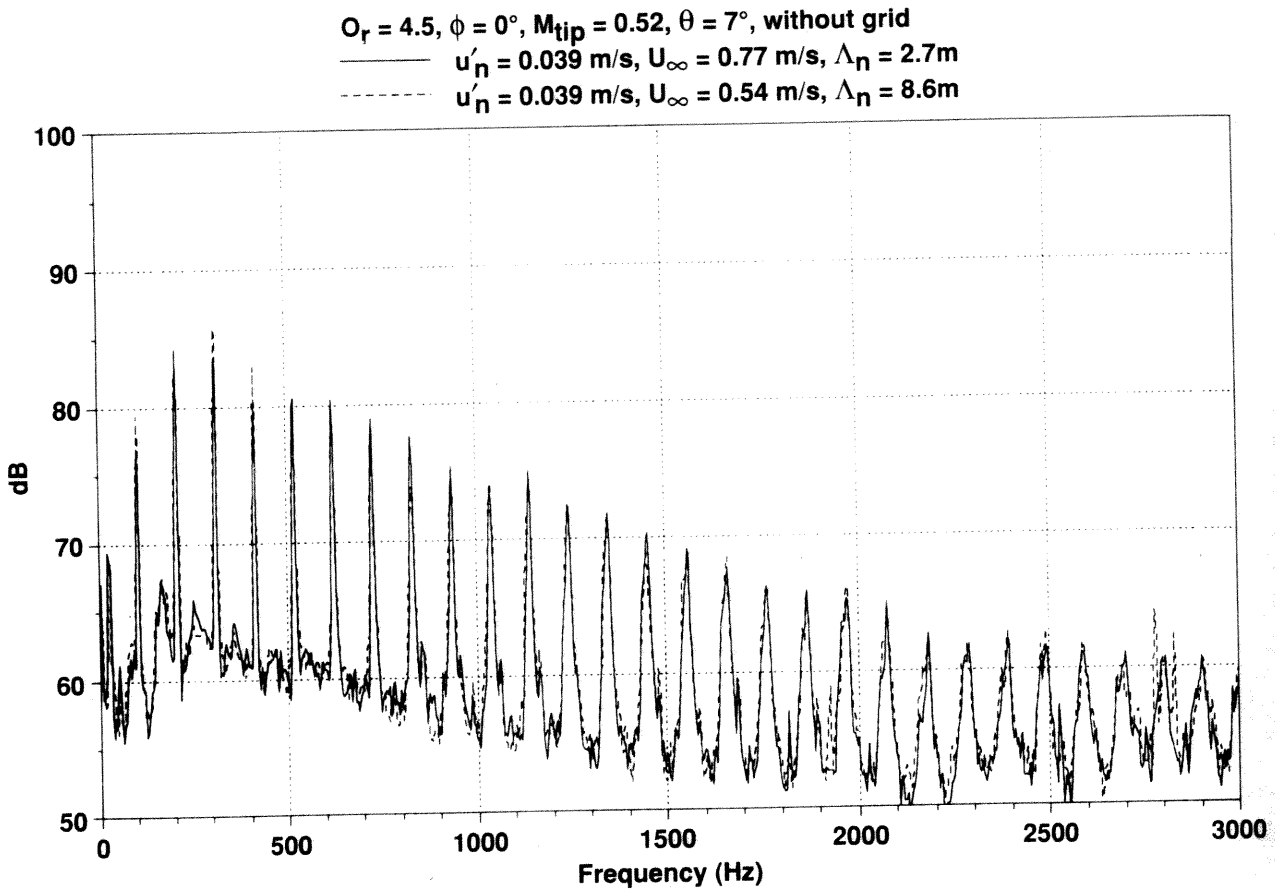

Fig. 16 Effect of near-field eddy length on acoustic power spectra at microphone 9.

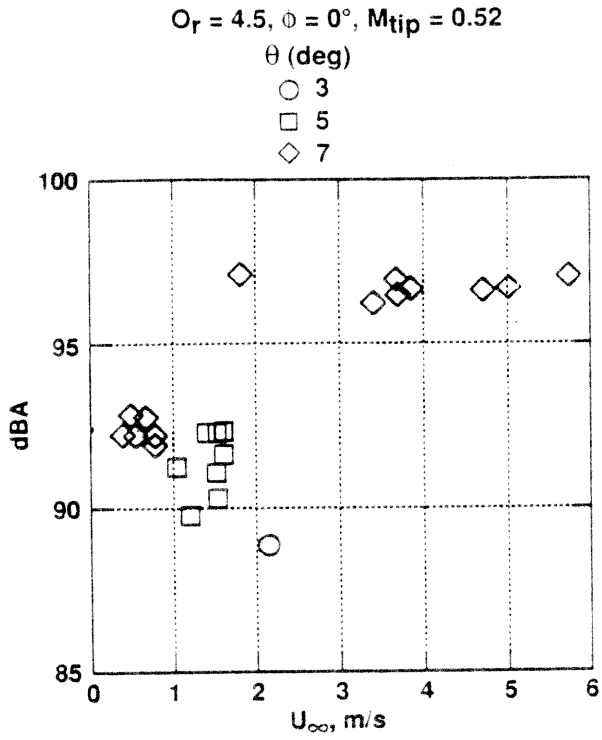

Fig. 17 Measured sound level variation with atmospheric wind speed at microphone 9.

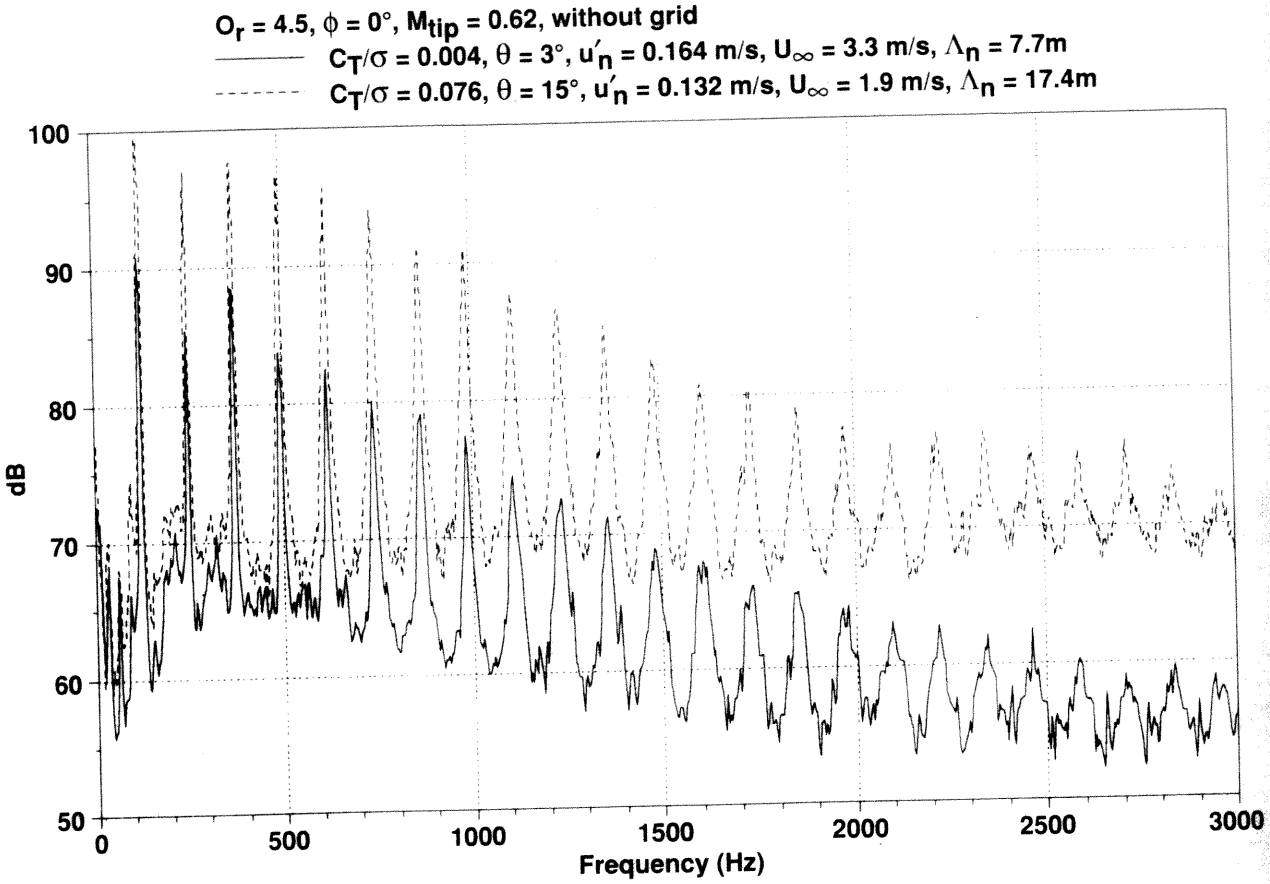

Fig. 18 Effect of C_T/σ on acoustic power spectra at microphone 9.

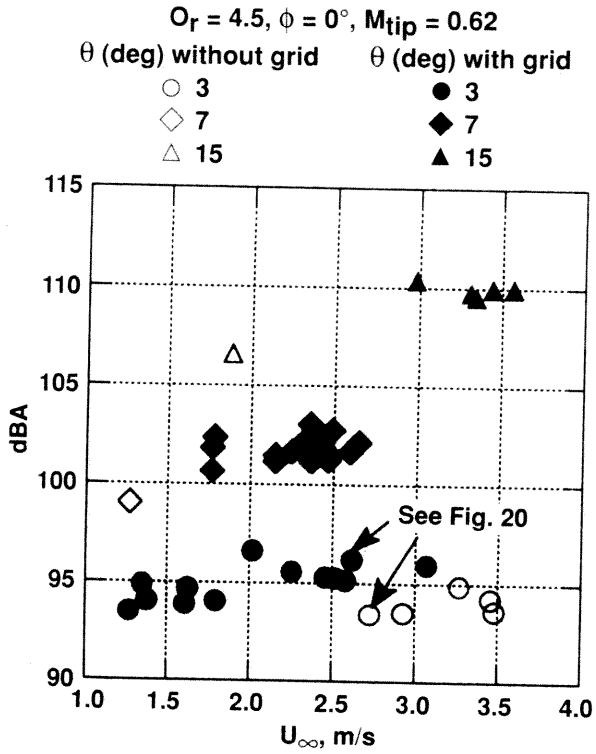

Fig. 19 Effect of grid on measured sound level at microphone 9.

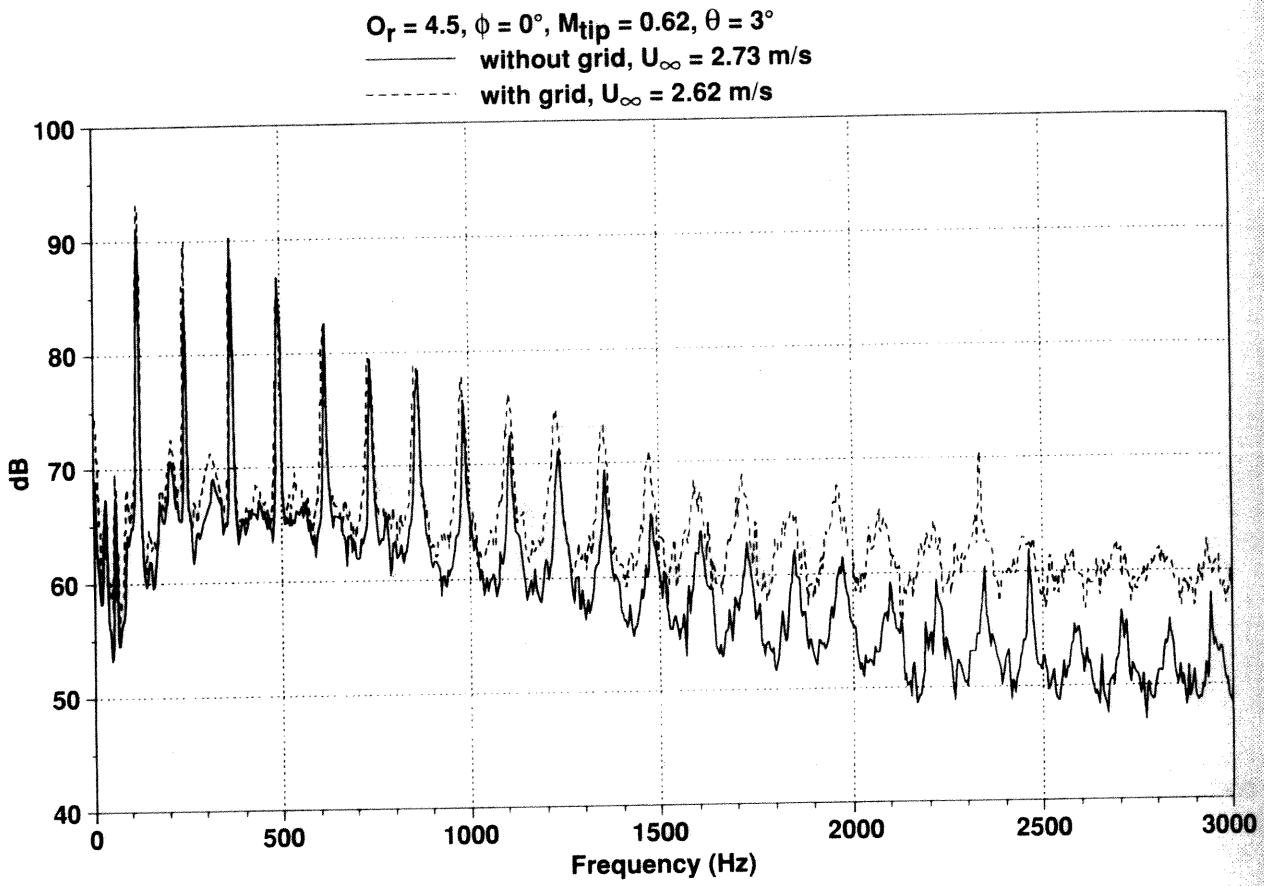

Fig. 20 Effect of grid on acoustic power spectra at microphone 9.